

Mathematical Morphology-Based Fault Detection in Radial DC Microgrids Considering Fault Current from VSC

Marija Čuljak, *Student Member, IEEE*, Hrvoje Pandžić, *Senior Member, IEEE*, and Juraj Havelka, *Senior Member, IEEE*

Abstract—The paper proposes a fast fault detection method for radial DC microgrids established on mathematical morphology (MM) denoising filters and detection principles utilizing only local measurements. The proposed fault detection algorithm utilizes the DC fault current signal from a Voltage Source Converter (VSC) and detects a fault. Problems related to communication delays are thus avoided, while preserving the low cost and computational burden.

The proposed fault detection framework includes five different MM-based denoising filters, employed as pre-signal processing methods whose features are assessed and compared. The influence of selecting an appropriate type and length of a structuring element (SE) on the proposed method is analyzed. The developed fault detection method based on MM is used for extracting transient features and detecting pole-to-pole (PP) and pole-to-ground (PG) faults within milliseconds of their occurrence. The proposed method is demonstrated using simulation tests in MATLAB/Simulink. The results indicate that the proposed method enables reliable, accurate and fast detection of both the PP and the PG faults. Computer simulations are carried out to verify that the proposed method distinguishes faults from overload.

Index Terms—voltage-source converter, fault detection, denoising filters, mathematical morphology, DC microgrid

I. INTRODUCTION

Multi-terminal DC (MTDC) microgrids are a new concept in electrical power system elements that connects multiple converters with DC lines in mesh or radial topologies. They are considered as one of the best solutions for integrating low-carbon DC sources such as photovoltaics (PVs), wind, fuel cells and battery storage systems [1], [2]. At the same voltage level, more power can be transmitted through DC lines and power losses are lower than in AC lines because DC cables are not subject to the skin effect. Further, the number of conversion stages is reduced. Hence, DC microgrids can increase the operational cost-effectiveness, energy efficiency, reliability and offer higher safety. However, there are many challenges for system protection within DC microgrids due to

a lack of reliable protective schemes [3]. The challenges can be summarized as follows:

- Peak value of a DC fault current and its raising rate-of-change usually have high values in comparison to the AC microgrids because of small impedance in LVDC systems [4].
- The issue of breaking a DC current because of the absence of natural zero-crossing points, which is typical for AC systems [5], [6].
- Challenges due to various grounding strategies [7].
- Fault resistance has a high impact on the sensitivity of the fault response [8].

Main requirements when designing an appropriate fault detection strategy are cost, computation burden, simplicity, speed and reliability. DC microgrids are connected to AC systems through converters with bidirectional power flow, mostly voltage-source converter (VSC). VSCs do not protect against DC fault currents. Various DERs with DC/DC power converters have different fault responses that cause issues with operation, fault detection and fault identification [9]. To develop an effective fault detection method, these fault responses should be analyzed and simulated in great detail. Fault currents in DC systems have steady state values, unlike the AC systems where arcs are extinguished naturally at the first crossing of the current through zero [10]. Hence, the DC microgrids' protection framework is a combination of a DC circuit breaker, fault detection relays, and measurement units, including advanced protection methods [11].

A. Related Work

In recent years, the lack of proper protection methods in DC microgrids was predominantly addressed by modern/hybrid methods instead of the conventional ones. Conventional protection schemes consist of the overcurrent protection, distance protection, differential protection, voltage protection, frequency protection and a combination of communication-based protection schemes [2].

Communication-based fault detection strategies, such as current differential methods, are proposed in [12], [13]. The method proposed in [12] requires two end measurements and a synchronized relay operation through the communication channel. The method described in [13] consists of a segment controller that has master and slave controllers which monitor the currents and control the separation of a faulted network segment. These methods have high sensitivity, however, they

M. Čuljak is with KONČAR – Electrical Engineering Institute Ltd., while H. Pandžić and J. Havelka are with the University of Zagreb Faculty of Electrical Engineering and Computing, Zagreb, Croatia.

This work was funded by the Croatian Science Foundation and the European Union through the European Social Fund under project Flexibility of Converter-based Microgrids – FLEXIBASE (PZS-2019-02-7747). It was also funded by the European Union through the European Regional Development Fund for the Competitiveness and Cohesion Operational Programme 2014–2020 of the Republic of Croatia under project No. KK.01.1.1.07: “Universal Communication and Control System for Industrial Facilities”.

require a proper communication link between the sensors for accurate fault detection. Moreover, a large number of measurement units is required and the complexity of the communication system increases the overall system cost [14]. Due to low magnitudes of PG currents, which are a consequence of high fault resistance, these studies cannot guarantee the PG fault detection.

Distance protection is quite common in AC systems, however, in DC systems it has limited accuracy for short lines, it is costly and highly sensitive to fault resistance.

Recently, signal processing methods have been adopted as reliable techniques for DC fault protection. These methods are based on extracting the signal faulty features using signal processing techniques such as Fast Fourier Transform (FFT), Wavelet Transform (WT), Hilbert-Huang Transform (HHT), Variational Mode Decomposition (VMD) and Mathematical Morphology (MM) [11], [15]–[18]. FFT is predominantly used, but its major drawbacks are low time-frequency resolution and distorted signals [4]. Another disadvantage is that it cannot be used for non-stationary signals.

WT-based methods decompose signals in frequency components with different resolution levels. The method presented in [19] is suitable only for pole-to-pole (PP) and not for pole-to-ground (PG) faults. Hence, the WT method is highly sensitive to harmonics and noise, which imposes higher computational requirements. In [15], HHT was applied to HVDC system distance protection in which the frequency of the DC voltage transient oscillation, calculated using the HHT, is used to estimate the fault distance from the circuit breaker to fault location. The main feature of HHT is to provide the instantaneous amplitude and frequency of the signal components. However, there can be a problem when intermittent waves occur at a lower-frequency signal [20]. VMD-based fault detection scheme was proposed in [21], where the most significant mode containing the maximum information was selected and the energy of that mode was computed. VMD is a non-recursive method that divides the signal into a finite number of sub-signals called intrinsic mode function. The challenge related to this method is the influence of noise, which should be taken into account as the energy of white noise is unavoidably contained in each bandwidth of the frequency spectrum part [22].

MM is a non-linear method widely used in various fields, such as signal and image processing, as well as power system transient analysis and protection. MM was applied to AC transmission and distribution systems [23]–[25]. In [26], [27], MM was employed to protect HVDC systems. A one-dimensional version of the MM method can be used for islanding detection [28], [29], noise filtering [30], detection of current transformer saturation [31] and monitoring of power quality events [32]. Compared to FFT and WT, MM is fully in the operational time zone, i.e. no time-frequency transformation is required, and uses non-complex operators [4]. Reference [33] proposes two signal-processing fault detection methods, one in the time domain and the other in the frequency domain. It compares their performance in terms of fault detection time, sensitivity to fault parameters, impact of sampling frequency, and computational speed. The conclusion is that the time domain method is economical, highly reliable and fast at detecting

faults. However, PG faults are not considered in [33]. In [34], a fault detection method based on two different MM filters for Low Impedance Faults (LIFs) and High Impedance Faults (HIFs) is applied to a DC ring microgrid. However, it considers solely the PP faults at the load side. Furthermore, in [35] detection of HIF in low-voltage DC systems is performed using MM. However, the needed time for fault detection during maximum fault resistance is 1 s, which is inapplicable to real-time systems. For further reading, a short overview of MM applications and MM-based methods is available in [4].

B. Contribution and Paper Organization

Considering the literature reviewed above, to overcome the discussed shortcomings, we further investigate the DC fault analysis and detection method on a multi-feeder radial low voltage DC microgrid with integration of distributed energy resources. We propose a scheme that detects faults in the shortest possible time without any required communication channel as it utilizes the fault current from the VSC line. First, the MM-based denoising filters are developed in pre-signal processing. Then, utilizing the MM features of the high-frequency signals caused by the power system, disturbances are extracted to distinguish between normal and fault conditions with high accuracy. The proposed method uses simple mathematical operators that have low computational burden and considers random background noise that may be contained in current fault signals. Our simulation results, with different fault resistances and locations, demonstrate the efficiency and accuracy of the proposed method.

Our method requires no communication link, avoiding issues related to data loss, delays, long response times, additional cost and communication failures. As it is highly computationally efficient, the method provides quick and effective fault detection. Low sampling rate of 10 kHz for current signal is used, which is essential for cost-effective current sensors selection.

Considering the above, contribution of this paper can be summarized as follows:

- Analysis and validation of several MM denoising filters tested for DC microgrids.
- Development of a fast MM-based fault detection method for DC microgrids using current signal from a single measurement point with enhanced speed and reliability.
- Detailed analyses and simulations of PP and PG faults at different locations in the DC microgrid (note that we do not detect location of the fault, only its occurrence).

The remainder of the paper is structured as follows. Section II analyzes PP and PG faults in DC microgrids. Section III presents general features of the MM, including principles of signal filtering and fault detecting, as well as the determination of the threshold and sampling frequency of the proposed method. In Section IV, an accurate representation of the DC microgrid components is provided, as well as the selection of an appropriate denoising filter and corresponding type and length of SE for the proposed denoised filter. The effectiveness and accuracy of fast fault detection method is verified on simulations in MATLAB/Simulink, considering different parameters such as fault location, fault resistance, fault types

and various operating points. Finally, Section V concludes the paper.

II. FAULTS IN DC MICROGRIDS

Faults in DC microgrids with DERs are divided in two types: PP, also called short-circuit faults, and PG, otherwise known as ground faults [9]. However, the processes of PP and PG faults are very similar. With respect to the fault response time, any fault in a DC microgrid is divided into two different parts: the transient and the steady state part [4]. DC-link capacitors of converters and cable discharge are responsible for the transient part, while the steady state is injected from power sources [36]. The transient fault response is described by defining three stages for PP faults, including the capacitor discharge stage (natural response), the diode freewheel stage (after $v_c = 0$, natural response), and the grid-side current-feeding stage (forced response). On the other hand, PG faults can be analyzed using two transient stages: the capacitor discharge and the grid-side current-feeding stage. In microgrids with a VSC interfaced to the AC side through an inductor (L_{conv}) and to the DC side through a capacitor (C), as shown in Figure 1, challenges related to the fault response of the VSC arise.

From the VSC side, when a PP fault occurs at t_0 , first the DC-link capacitor discharge stage is started. The capacitor of the DC circuit becomes a DC source and begins to exponentially discharge current through the impedance of the lines. The magnitude of the peak current becomes several hundred times higher than the nominal current and is much higher as compared to the AC systems. DC fault behaviour can be presented as a second-order RLC circuit comprised of a DC filter capacitor of converter, a stray capacitor value and a line impedance from the capacitor source to the fault location, which in return have impact on the fault resistance, type and location [37]. Consequently, the VSC converter has high fault contribution as compared to DC/DC converters due to a much larger filter. Moreover, IGBT switches of the VSC are cut off for self-protection [38].

The diode freewheeling stage begins after the capacitor discharge stage, i.e. when the DC circuit voltage drops to zero or takes a negative value. In the event of a P-G breakdown, current will not flow through the diodes because the capacitor voltage of the DC circuit will not drop to zero. During the second stage of a PP fault, the voltage at the VSC terminal becomes reversed and the fault current starts flowing through forward-biased freewheeling diodes at critical time t_1 [39]. This critical time should be the upper limit on operation of both the main and the backup circuit breakers [40]. The impact of a DC fault on freewheel diodes in the VSC and DC/DC converters can be dangerous due to an increased inductive component in the discharge path, considering that there is no preventive discharge protection [40]. This stage is the most challenging for the VSC freewheel diodes. Thus, any fault should be detected before t_1 , i.e. before dropping the capacitor voltage to zero, to avoid rapid damage to the diodes. Considering the described transient behaviour of fault currents and possible repercussions during PP faults, any faults should

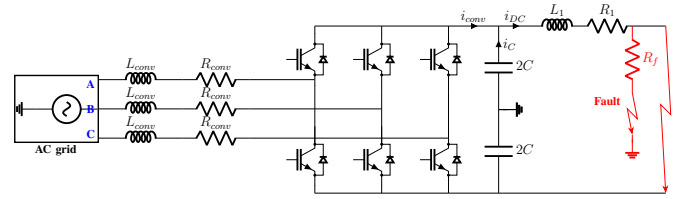


Figure 1: Equivalent scheme of a VSC under PP and PG fault

be detected in a very short time interval. Thus, it is necessary to operate relays in a specified time interval, defined as a difference between t_1 and the Overall Fault Clearance Time (OFCT). This difference is named IPDM and can be calculated as follows (1):

$$IPDM = t_1 - OFCT = t_1 - t_0 - t_B \quad (1)$$

where t_B is the operation time of the breaker.

During the grid-side current feeding stage, the VSC acts as an uncontrollable rectifier due to the blocked IGBTs. The contribution from the converter can be calculated using a three-phase short circuit analysis and the fault current at this stage is presented in [40].

In the steady state part, the DC currents and voltages transition to a stable stage as the AC side contribution to the fault current is significantly reduced. The steady fault current depends on the resistance and inductance of the fault circuit, the DC-link capacitance and the angular frequency of the equivalent voltage source.

Detailed analyses for PP and PG faults in the DC microgrid can be found in [40], [41].

III. MATHEMATICAL MORPHOLOGY

MM is one of the non-linear signal processing techniques which has been primarily used for image processing. Unlike most frequency-domain signal processing techniques such as FFT, WT and HHT, which use complex calculations, MM depicts the signal profile directly in the time domain [26]. It extracts signal features like shape, format and length in the time domain and uses simple arithmetical calculations such as the subtraction, addition, minimum and maximum operators, without division or multiplication [27]. Additionally, it is simpler than the above-mentioned methods because of the MM filter ability to process lower sampling frequencies. Although this method can be applied for fault detection, classification and location in both the AC and the DC power systems, it is more convenient for DC systems because only the current or voltage magnitudes need to be categorized, whereas for AC system the need for individual phase current measurement and phasor comparison increases the operating time [42].

Structuring element is a predefined shape used as a probe for the extraction of relevant features of the original signal. It is a fundamental component of all MM calculations and may have different geometrical shapes considering the target application. Selection of an appropriate shape, height and length of the SE should be performed carefully because transformations using the MM methods rely on the choice of SE. Type, frequency content and sampling rate of the distributed signal under examination is used to determine the shape of the SE [43].

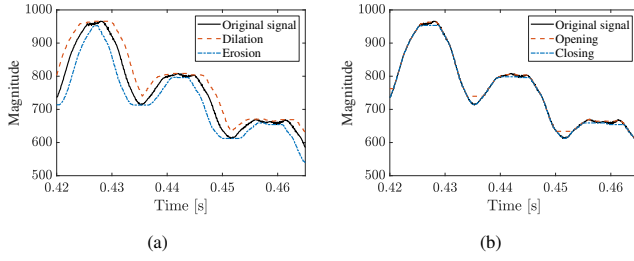


Figure 2: Results of: (a) dilation and erosion operators, (b) opening and closing operators in signal processing

Generally, shapes of SE can vary from regular to irregular curves. The function of SE in MM is similar to the function of windows in the frequency domain signal processing methods and its selection mainly depends on the used MM operators [43]. As MM is a non-linear method, there is no classical optimization method for selecting the optimal SE.

In this paper, the first step is introducing the basic MM operators that depict fundamental structures of a signal.

A. Operators

Fundamental transformation operators of MM are dilation and erosion [44]. All other filters and advanced operators are their combinations. Suppose $f(n)$ denotes an input signal and $g(m)$ is an SE whose length is shorter than that of f . Dilation and erosion can be defined as:

$$\delta(f) = (f \oplus g)(n) = \max\{f(n-m) + g(m)\}, \quad (2)$$

$$0 \leq (n-m) \leq N, m \geq 0$$

$$\epsilon(f) = (f \ominus g)(n) = \min\{f(n+m) - g(m)\}, \quad (3)$$

$$0 \leq (n+m) \leq N, m \geq 0$$

where, N is the total number of samples of N . Dilation is a swelling or an expanding procedure, while erosion is a shrinking procedure. Hence, an SE with its origin and a sample of the signal within the window can be presented [32]:

$$(f \ominus g)(n) \leq f \leq (f \oplus g)(n) \quad (4)$$

Dilation and erosion functions are visualized in Figure 2a.

Other commonly used operations for one-dimensional signals are opening and closing. These are mainly used for flattening the spiky boundaries and filling the gaps in signals. Opening performs a dilation on an eroded signal by the same SE. On the other hand, closing performs an erosion on a dilated signal using the same SE in both operations. Equations for opening and closing operators are:

$$\gamma(f) = (f \circ g)(n) = ((f \ominus g) \oplus g)(n) \quad (5)$$

$$\phi(f) = (f \bullet g)(n) = ((f \oplus g) \ominus g)(n) \quad (6)$$

The results of opening and closing are given in Figure 2b.

Within the framework of this paper, the noise should be eliminated with proper MM-based filters to ensure an effective extraction transient of the fault signal. Meanwhile, the shape information of the signals should not be affected [44]. As they present the main contribution of this paper, the denoising filters and the method proposed for fault detection are explained in the following subsections.

B. Signal Filtering Principle of Mathematical Morphology

Power signals often contain complex and altering noise which decreases accuracy of the measurements. Most filters cannot reduce noise without affecting the signal performance.

There are no previous works where MM-based denoising filters are applied to low-voltage DC power signals. Thus, we first examine and apply filters already used for HVDC signals from the existing literature. Based on four basic MM operators, i.e. erosion, dilation, opening and closing, various filters have been developed for suppressing the noise in several applications. Morphological median filters (MMF) have been applied mainly to suppress impulse noise whose probability density has heavier peaks than the Gaussian for the signal enhancement, since they can remove this type of noise without losing geometric shapes, as would be the case for linear filtering. Consequently, MMF is a common filter that provides good results in denoising power system signals at the preprocessing stage, i.e. before detection of different kinds of transients and disturbances. To filter noise from the test-signal, literature recommends averaging the dilated and eroded signals, called MMF1 and averaging opening and closing signals, called MMF2. These two types of MMF are defined as:

$$MMF1 = \frac{(\delta(n) + \epsilon(n))}{2} \quad (7)$$

$$MMF2 = \frac{(\gamma(n) + \phi(n))}{2} \quad (8)$$

MMF3 filter is also called OCCO in some papers, as it is composed of the Opening-Closing (OC) and the Closing-Opening (CO) filters [27]. OC and CO filters are given as:

$$OC[f(n)] = (f \circ g \bullet g)(n) \quad (9)$$

$$CO[f(n)] = (f \bullet g \circ g)(n) \quad (10)$$

These two filters are connected in a cascade to form MMF3:

$$MMF3 = \frac{(OC[f(n)] + CO[f(n)])}{2} \quad (11)$$

Except of median filters used for suppressing the noise in low voltage signals, we include two additional filters (CDE_OED and DCE_EOD), presented in [45], which have better filtering aspects than MMF1, MMF2 and MMF3 (OCCO). These filters are composed of four new cascaded operators, i.e. CDE , OED , DCE and EOD , which improve the ability to extract positive and negative impulses from a signal:

$$CDE[f(n)] = (f \bullet g \oplus g \ominus g)(n) \quad (12)$$

$$DCE[f(n)] = (f \oplus g \bullet g \ominus g)(n) \quad (13)$$

$$EOD[f(n)] = (f \ominus g \circ g \oplus g)(n) \quad (14)$$

$$OED[f(n)] = (f \circ g \ominus g \oplus g)(n) \quad (15)$$

To extract positive and negative impact components simultaneously, the average sums of CDE & OED and DCE & EOD are generated as:

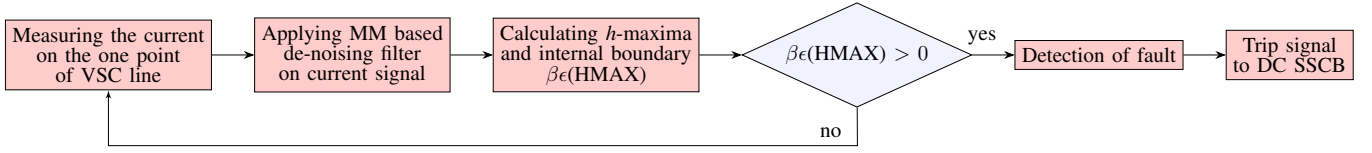


Figure 3: Flowchart of proposed detection method

$$CDE_OED = \frac{CDE + OED}{2} \quad (16)$$

$$DCE_EOD = \frac{DCE + EOD}{2} \quad (17)$$

C. Detection Principle of Mathematical Morphology

There are various MM-based methods to detect power quality problems and transient-like faults in power systems. Morphology gradient is one of the techniques in detecting the edge of an image or a signal [32]. Beucher gradient is the most frequently used morphological gradient:

$$\rho_B(f) = \delta(f) - \epsilon(f) = (f \oplus g) - (f \ominus g) \quad (18)$$

It is composed of two operators – the internal and the external boundary. They are often called half-gradients. The internal boundary or the half-gradient by erosion is given as a difference of the original signal and the eroded signal:

$$\beta_\epsilon(f) = f - \epsilon(f) = f - (f \ominus g) \quad (19)$$

The external boundary or half-gradient by dilation is defined as a difference between the dilated signal and the original signal:

$$\beta_\delta(f) = \delta(f) - f = (f \oplus g) - f \quad (20)$$

Even though Beucher gradient generally has good properties in terms of noise immunity, it often needs more time to extract the signal changes. Half-gradients by erosion or dilation (internal and external boundaries) are good choices for this application because of their relative noise immunity. However, the most valuable feature is low detail losses of the signal, which is very important for disturbance and fault recognition. The Beucher gradient peaks are located at the edges, but the internal and external gradients are located at each side of the edges. The choice between the internal and external gradients depends on the nature and the waveform of the signal to be extracted. The reason for using the internal boundary instead of the external one is emphasizing the edges of the signal while ignoring the surface around. Additionally, the external boundary could falsely trip in case of sudden load changes or minor disturbances because of faster changes in the output as compared to the internal one. In this paper, the first step is to calculate the h -maxima transform of the filtered signal and then use it with the internal boundary function to detect the transient signal features. The main goal of the h -maxima transform in morphology is the extraction of a regional maxima while suppressing all maxima in the signal whose height is lower than H , decreasing the height of the remaining maxima by H , where H can be considered as a threshold value.

After calculating the h -maxima, the extracted peaks can be given using the internal boundary or the half-gradient by erosion:

$$\beta_\epsilon(HMAX) = HMAX - \epsilon(HMAX) \quad (21)$$

Therefore, using h -maxima and internal boundary a fault can be detected before the magnitude of a fault current reaches its maximum within the first milliseconds of the fault. A flowchart of the proposed detection method is provided in Figure 3 and consists of the following steps:

- 1) Step 1: Measuring the current on one side of the VSC line and loading data from the signal into a window of pre-defined size (12 samples).
- 2) Step 2: Applying an MM-based denoising filter to the current signal to reduce noise at the preprocessing signal stage by a measuring relay (R).
- 3) Step 3: Calculating the h -maxima of the denoised current signal by a measuring relay (R).
- 4) Step 4: Calculating the internal boundaries, where the input signal is the calculated h -maxima, used to detect transient signal features by a measuring relay (R).
- 5) Step 5: If the output value of the calculated signal is higher than zero, it is in the fault mode, otherwise it is in the normal operation mode.
- 6) Step 6: Send trip signal to the Solid-State Circuit Breaker (SSCB).

1) *Threshold Determination:* Finding a reasonable threshold in DC microgrids is still an open question as it cannot be computed exactly. However, a good approach is to predict/anticipate the maximum loading conditions for a particular DC microgrid setup and to define the threshold based on these predictions. In the paper, a predefined threshold is H and is used as a function in the h -maxima transform where all maxima in the signal whose magnitude is lower than H are suppressed. The faults are detected when the value of the internal boundary, which is a function of the h -maxima, is greater than zero. The threshold value is selected to meet the main conditions proposed in [46]: i) sensitivity to a high-resistance (up to 20 Ω) and far-end faults that result in small transients (F3 and F4); ii) higher current magnitude and faster current slope than the non-fault disturbances, and iii) employing a sufficient protection margin. Thresholds for both types of faults are derived based on system studies conducted under severe scenarios. The system studies consisted of determining the currents for different operating points. As the value of the threshold depends on the current through the VSC cable, it is observed that the value of i_{DC} at the instant of the fault ($t = 0$) depends on P_{ref} (value of the active power shared between the microgrid and the AC grid, range from -10 to 10), R_f (fault resistance), and I_L (current through the inductance).

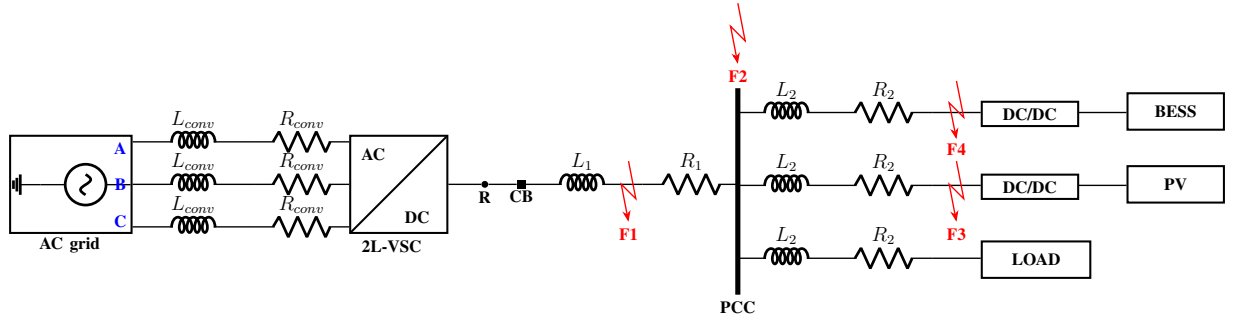


Figure 4: Layout of DC microgrid with possible fault locations, MM-based measurement relay (R) and circuit breaker (CB)

The value of H is set to 2.2 based on the most sensitive case observed for a PG with high fault resistance at location F4, i.e. the farthest from the relay located at the VSC line. This case results in the smallest current magnitude change (with the largest time-delay, considering the used windows). The current magnitude changes are calculated over a fixed time interval using windows (12 sampled values) and these changes will be compared to a predefined current threshold. At the same time, the selected value of H ensures a sufficient margin to not to trip the circuit breaker upon minor disturbances such as sudden load changes or external disturbances.

2) *Sampling Frequency Determination*: The choice of sampling frequency is closely related to the frequency base domain such as WT and STFT, because decreasing the sampling frequency causes performance degradation. On the other side, the MM method is hardly influenced by this factor and does not require high sampling for signal detection in DC microgrids [33]. Sampling frequency of today's digital relays is 10 kHz. Although, 10 kHz can be considered a low sampling rate, one would prefer to use lower sampling frequency for the economic reasons. Hence, the MM method is the most cost-effective in that sense [33]. Lower sampling rate also reduces the window length and the calculation burden. As long as the SE is chosen rationally, higher sampling rate does not necessarily yield better output. Consequently, due to the local structure of the proposed method, the sensors with 10 kHz sampling rate are required and satisfactory for the purpose of our study.

IV. CASE STUDY

A. System Description

The case study DC microgrid is implemented in MATLAB/Simulink. Figure 4 shows a single-line diagram of the studied radial DC microgrid and possible fault locations indicated as F1-F4. The mid-point grounding system is used to ensure operation at different voltage levels: 500 V, +250 V and -250 V which are within the LVD 2014/35/EU range, i.e. 75 V–1.5 kV [47]. The mid-point DC configuration provides an advantage over the one-pole as it enables a bipolar structure and clears faults faster.

1) *Model of the Two-Level VSC*: VSC techniques are commonly used for AC/DC or DC/AC power conversion. Grid-following type of converters should be perfectly synchronized with the AC voltage to regulate the active and reactive power exchange with the system. They are represented as an ideal

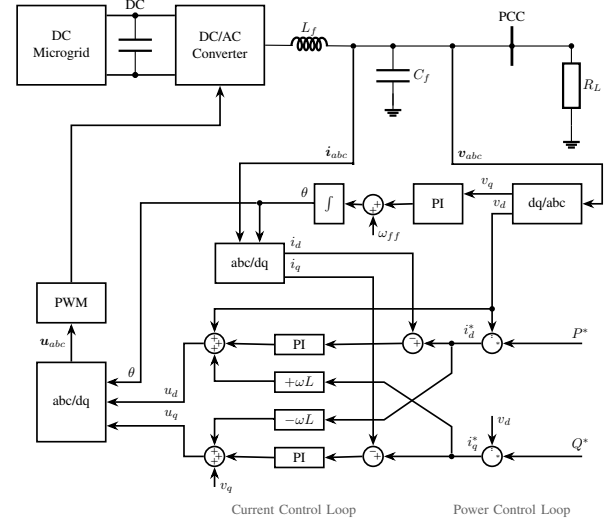


Figure 5: Control of a two-level VSC

current sources in parallel with high impedance, and connected to the grid [48]. They are able to operate in parallel with other grid-following converters in the grid-connected mode because of high equivalent output impedance [49]. Most converters used with non-dispatchable micro-generators (e.g. PV arrays), operate in the grid-following mode [48], [49].

The circuit of a two-level VSC (2L-VSC) consists of six switching devices, typically insulated-gate bipolar transistors (IGBTs), and a DC-link capacitor. The presence of these active switches with a proper control scheme and line filters enable generating sinusoidal current, adjustable power factor and bidirectional power flow [49]. Control of grid-following units can be described in different reference frames, such as dq synchronous reference frame or $\alpha\beta$ stationary reference frame [48]. In this paper, the dq reference frame is used as it is widely applied in three-phase systems. Grid-following converters require measured currents and voltages at the AC side, which are converted using the Park transformation from a three-phase (abc) signal to the $dq0$ synchronous reference frame. Then, the voltage and current references are passed through a first-order discrete low-pass filter to attenuate the switching harmonics in the measurements. The inner current controller of grid-following converters regulates the current injected into the grid, while the external controller sets a reference value of the current for power regulation injected into the grid, as shown in Figure 5.

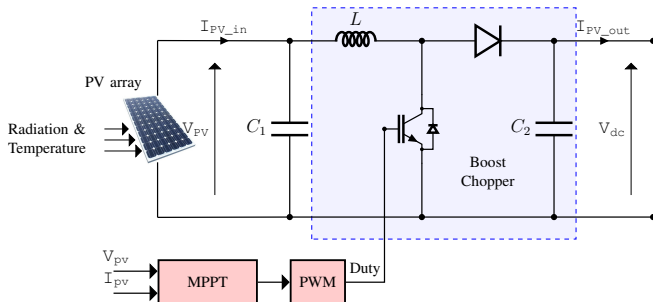


Figure 6: Model of a PV system and its control

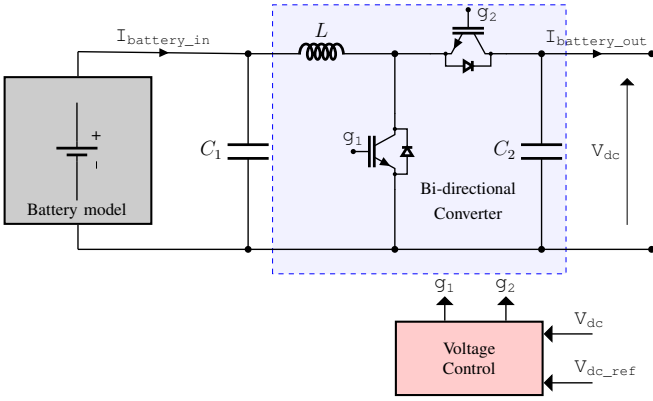


Figure 7: Model of the BESS and its control

2) *Model of the PV System with a DC/DC Boost Converter:* A 6 kW PV array is modelled using an in-built library model in MATLAB/Simulink and connected to a DC-DC boost converter, as shown in Figure 6. This DC/DC converter enables the PV system to operate at its maximum power point (MPP) and adapt the DC array voltage to the DC-bus voltage. An improved incremental technique is used to track the peak power under fast-varying atmospheric conditions.

The PV current and voltage are inputs to the boost converter, while its output is the voltage obtained from correlation with the maximum power. Switching frequency of the pulse-width modulation (PWM) is set to 25 kHz to avoid high-frequency parasitic elements and noise.

3) *Model of the BESS with a DC/DC Bidirectional Converter:* A lithium-ion battery energy storage system (BESS) with 12 kWh capacity is connected to a bidirectional buck-boost converter, as shown in Figure 7.

The main purpose of the bidirectional buck-boost converter is to control the DC bus voltage using a PI controller at a constant value by measuring the DC bus voltage signal. This enables stable operation of the DC microgrid in both the grid-connected and the islanded operation modes. The measurement voltage is compared to the reference, the PI translates the error to a duty cycle in values between 0 and 1. Once the duty cycle is obtained, it is compared with a sawtooth signal to obtain pulses sent to the IGBT. This implies that this converter operates in two states: state-on-switch and state-off-switch.

B. Simulation Results for Filtering

To reduce the noise effect and simultaneously maintain the features of fault signals, in our work we analyze and compare

five different filters and assess the impact of the type and length of an SE in these filters. Simulations under various conditions are conducted to compare performance of the filters. Gaussian white noise of 60 dB was added to the fault current signal to be processed. First, we compare different types of filters presented in III-B.

Figures 8a–8e show the original signal and the signals after applying MMF1, MMF2, MMF3 (OCCO), CDE_OED and DCE_EOD filters. The dilation and erosion effects can clearly fill the top and bottom tips of the signal, respectively. Dilation expands a signal, while erosion shrinks it. However, applying dilation and erosion operators in MMF1 can distort a signal. Thus, in MMF2 the morphological opening operation is used to filter the peak noise above a signal, thereby resulting in a low output waveform amplitude. On the other hand, the closing operation is used to suppress the valley noise below the signal, thereby resulting in a high output waveform amplitude. However, open-closing or close-opening operations can lead to statistical deflections of the amplitude and the signal, i.e., the result of open-closing operation has lower amplitude than the original signal and the result of close-opening operation has higher amplitude than the original signal, which causes a signal distortion. Considering the mathematical operation characteristics of morphology and the requirements of eliminating harmonics in signals of a power system, the morphological opening operation is combined with the closing operation to construct a cascaded hybrid filter and improve the filtering accuracy. In this paper, we utilize an average weighted combination of open-closing and close-opening operation called OCCO. The OCCO filter is chosen primarily due to its effective combination of the basic morphological operators as well as for its extraction of bidirectional impulses. On the other hand, taking the average of the intermediate results obviously prevents the preservation of the initial waveform by smoothing it, which is not suitable for this application. CDE and DCE combine the dilation and closing operators on the signal to suppress negative impulses, while the erosion operator is used to correct the retained positive impulses. EOD and OED integrate erosion and opening operators to effectively suppress positive impulses of the signal, while the dilation operator corrects the retained positive impulses. First, to extract positive impulses and preserve the shape of the signal, the cascades of dilation, closing and erosion, i.e. closing-dilation-erosion (CDE) and dilation-closing-erosion (DCE), are defined. Second, to extract negative impulses and preserve the shape of the signal, the cascades of erosion, opening and dilation, i.e. erosion-opening-dilation (EOD) and opening-erosion-dilation (OED), are defined. As shown in Figure 8a, MMF1 causes a delay in the denoised signal and destroys the original signal. On the other hand, MMF2 has issues in preserving the waveform features of the original signal (Figure 8b). Figures 8c–8d indicate that the OCCO filter has almost the same effects on the signal as CDE_OED, which can be confirmed by the calculated RMSE and SNR values provided in Table I. The best performance in the framework of preserving the waveform characteristics and reducing the noise effect of the signal has DCE_EOD, as can be seen in Figure 8e. Also, the significant smoothing of the signal is

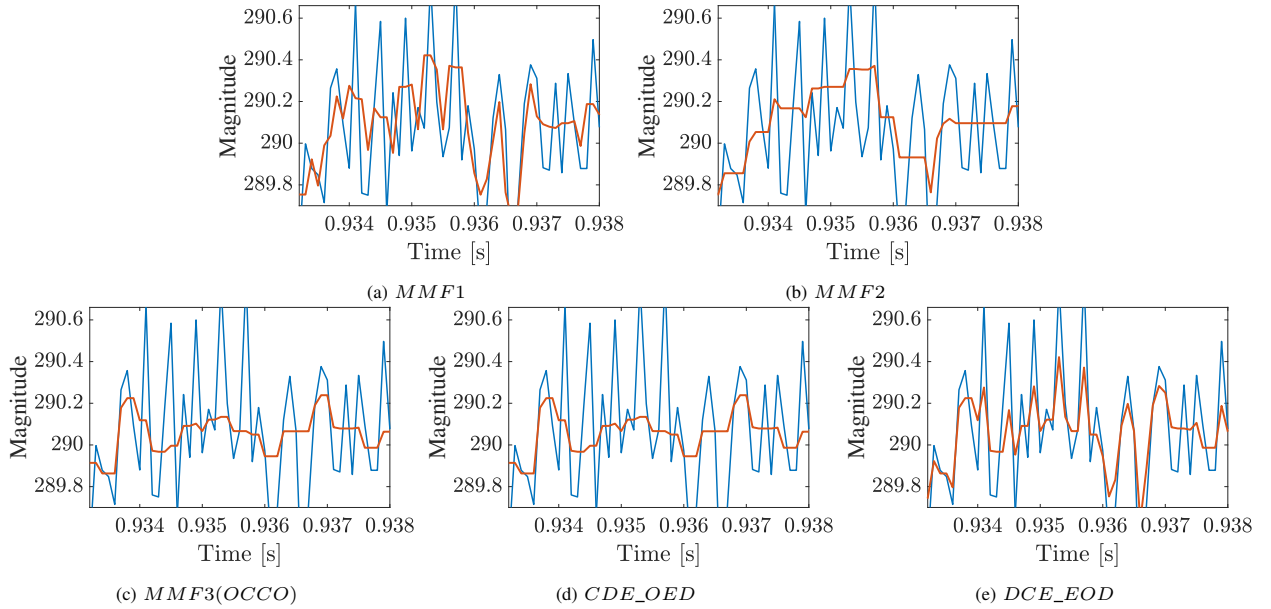


Figure 8: Simulation results for denoising filters [blue – current signal with noise, red – denoised signal]

TABLE I
RMSE AND SNR FOR DIFFERENT FILTERS

Filter type	RMSE	SNR
MMF1	0.2516	60.7586
MMF2	0.2027	62.6350
MMF3 (OCCO)	0.1935	63.0220
CDE_OED	0.1939	63.0227
DCE_EOD	0.1498	65.2610

TABLE II
RMSE AND SNR FOR DIFFERENT TYPES OF SE

SE type	Straight line	Diamond	Disc	Ladder	Semi-circular
RMSE	0.4222	1.3704	1.0373	0.3722	0.2965
SNR	60.1834	50.0221	52.3747	60.9305	61.2716

avoided using DCE_EOD filter. To prove and summarize the obtained results, Table I shows the calculated RMSE and SNR parameters, which demonstrate the best denoising impact of DCE_EOD filter on the original signal.

1) *Selecting an Appropriate Type of SE*: The next step was to study the type of SE for appropriate noise elimination and filtering. In this analysis, the length of SE is the same for all types ($l = 9$). Structuring elements with straight line (flat), diamond, disc, ladder and semi-circular shapes were used. Based on the Root-Mean-Square Error (RMSE) and Signal-to-Noise Ratio (SNR) of the selected types of SEs, the signals obtained with semi-circular and flat structural elements were identified to perform best, as can be seen in Table II. Based on the highest SNR value and the best RMSE value, the semi-circular SE is chosen as the filter parameter to be used in simulations.

2) *Selecting an Appropriate Length of the SE*: The SE length defines the size of the window and the delay in the filter output. This means that an increase in the length of the SE is always followed by an increased delay in the output [30], [43]. The delay of a filter can be calculated as:

$$FilterDelay = \Delta T \cdot (l_e - 1) \quad (22)$$

TABLE III
RMSE AND SNR FOR DIFFERENT LENGTHS OF SE

SE size	3	5	7	9	11	13	15
RMSE	0.3083	0.3083	0.3378	0.3629	0.4069	0.4752	0.6422
SNR	62.914	62.914	62.119	61.498	60.503	59.156	56.539

where ΔT is the sampling interval and l_e the SE length.

SE commonly does not have a large size (length) and the SE array values can be constant, increasing, decreasing, triangular, etc. The values are different according to the signal processing purpose, such as filtering, disturbance or transient detection. We conduct simulation studies for selecting a proper length of the SE, similar as for the SE type. The optimal SE length was determined based on the SNR and RMSE values given in Table III. Semi-circular SE of different lengths were used for the simulations. Thus, considering the RMSE, SNR, filter delay and other factors, a semi-circular SE with the length of three was selected for morphological filtering. The numbers in Table III indicate that increasing the length increases the RMSE as well.

According to these results, increasing the size of SE does not necessarily increase the accuracy of the results. The main drawback of a larger size SE is a distortion of the hidden signal and an increased sampling delay due to the morphology-based computations. Although the major peaks will be detected more clearly, lower peaks are not clearly visible by using a large-size SE.

C. Simulation Results for the Proposed Detection Method

Similar as in signal filtering, our detection method first needs to determine the type and length of the SE to ensure accurate and reliable detection. The selected type of SE in detection is straight line (flat) and the length is 20. A lengthy SE in the detection method is problematic as it requires much

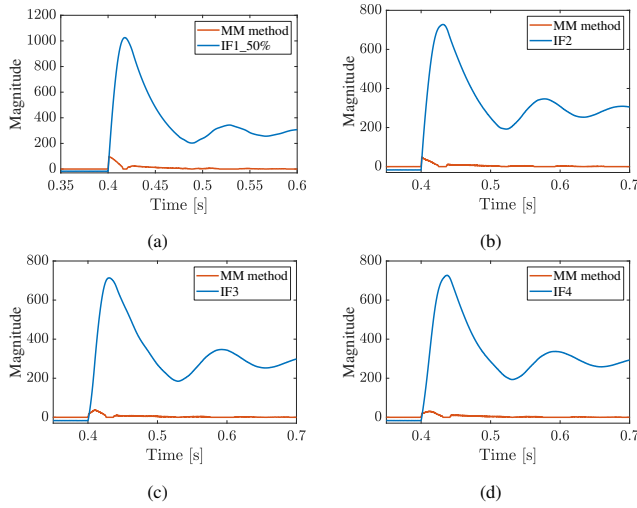


Figure 9: Applied MM detection method on fault current during a PP fault at different locations: (a) F1 – 50% of VSC line, (b) F2 – DC busbar, (c) F3 – PV system line, (d) F4 – battery system line

TABLE IV
IPDM RELATED TO DIFFERENT FAULT LOCATIONS DURING PP

Fault Location	t_1 [s]	IPDM [ms]	Max. fault current [A]
F1_10%	0.40997	9.37	2236
F1_30%	0.41838	17.78	1336
F1_50%	0.42603	25.43	1026
F2	0.43916	38.56	727.3
F3	0.44267	42.07	713.6
F4	0.44368	43.08	726.7

memory for data and can cause unwanted continuous disturbances. On the other hand, a short SE distorts the extracted features, yielding the method unreliable. Generally, the fault detection method relies on measuring the current, which only depends on the shared power between the DC microgrid and the main AC grid (through the VSC). Requirements on the voltage and the power flow are considered simultaneously at the point-of-common-coupling (PCC). Power management is based on controlling the power balance in the DC microgrid. If there is a lack of energy, it will withdraw the deficit from the AC grid and if there is a surplus energy produced by the PV, it will inject it in the AC grid. The battery regulates voltage at the DC busbar. Protective MM-based relay, which sends the tripping command to the Solid-state Circuit Breakers (SSCB), is placed at one side of the line between the VSC and the DC microgrid, as indicated in Figure 4. As indicated in Section III, the window length is $N = 12$ with sampling frequency of 10 kHz and the threshold is 2.2 considering the most critical case. Operational time of the SSCB-type fault isolating device is considered around $600 \mu\text{s}$, as defined in [50]. Communication links are not needed because the scheme requires only current of one side of the VSC line. The absence of communication links highly reduces the delay and noise. The fault path impedance fluctuates, depending on the fault location, while the fault resistance is variable, considering the type of fault. The main purpose of the study is to detect a fault at any place in the DC microgrid using a single measurement point. However, our method does not detect the fault location.

1) *PP Faults Detection*: Figure 9 shows fault currents as seen by relay R for different locations of PP faults in the

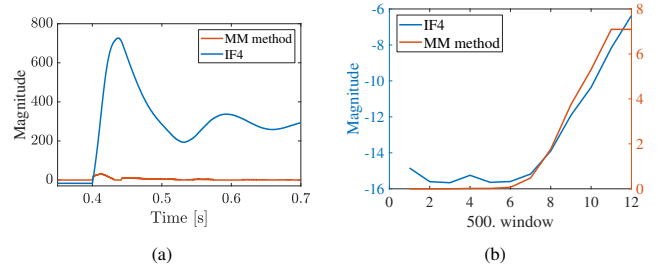


Figure 10: Results of the PP fault simulation: (a) MM method applied to the fault occurred at F4 - battery line ($R_f=0.05 \Omega$), (b) time window for the fault detection

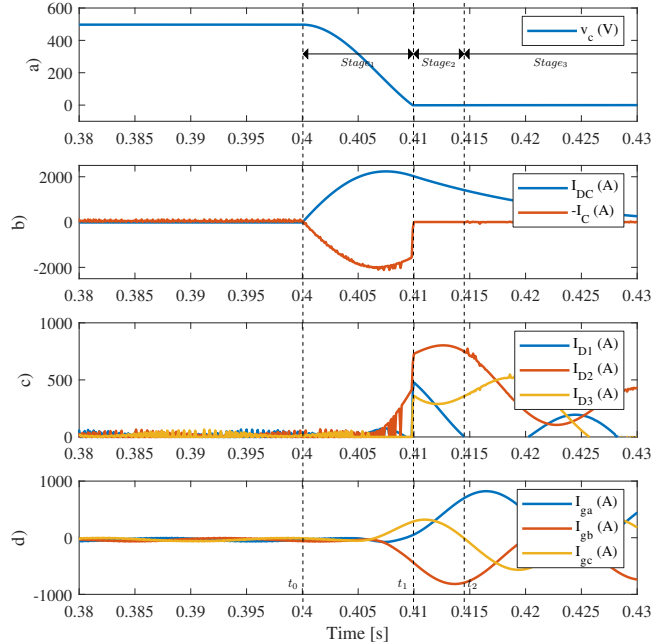


Figure 11: PP fault at the VSC line. a) DC link capacitor voltage v_c b) Current over the VSC line i_{DC} , and capacitor current i_c c) Three-phase diode current I_{D1} , I_{D2} , I_{D3} d) Three-phase grid-side currents I_{ga} , I_{gb} , I_{gc}

microgrid, while Table IV shows the calculated IPDM. The PP fault occurs at $t_0 = 0.4$ s. The results indicate the faults are always detected before IPDM in all scenarios and before the peak time of the fault current. As can be seen in Figure 10, the PP fault will be detected in the same window in which the fault occurs.

Figure 11 shows different stages during the PP fault at 10% of the VSC line. v_c is the voltage of the DC-link capacitor of the VSC, i_c is the current of the DC-link capacitor, and i_{DC} is the fault current equal to the sum of i_c and the line current before the DC-link capacitor of the VSC. I_{D1} , I_{D2} and I_{D3} are the freewheel diode currents of the VSC, while I_{ga} , I_{gb} and I_{gc} are three-phase grid currents. During Stage I, voltage v_c drops to zero while the transient current waveforms i_{DC} and i_c are similar to each other, which proves that the fault current is mainly supplied by the DC-link capacitor. Due to the first stage of the fault and the high-rise capacitive discharging current, $\beta_e(HMAX)$ signal immediately increases with the peak that is reached before IPDM. In view of different fault locations and fault path impedances, magnitude and time to

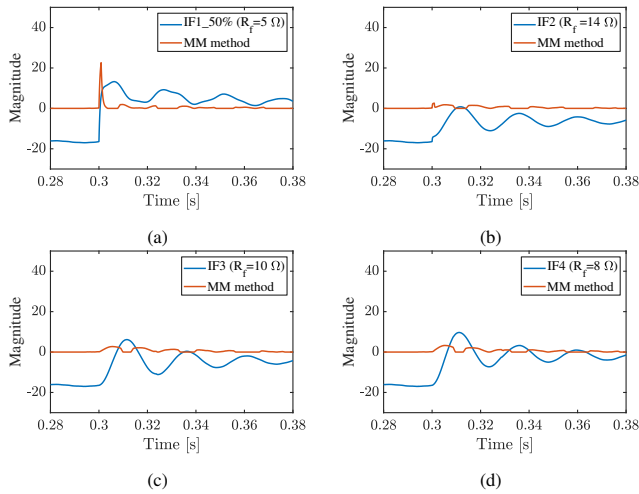


Figure 12: Applied MM detection method on fault current during a PG fault at different locations: (a) F1 – 50% of VSC line ($R_f = 5 \Omega$), (b) F2 – DC busbar ($R_f = 14 \Omega$), (c) F3 – PV system line ($R_f = 10 \Omega$), (d) F4 – battery system line ($R_f = 8 \Omega$),

reach the maximum is modified. Figure 11 shows that the DC-Link Capacitor Discharging Stage ends at $t_1 = 0.4099s$, while signal of the detection method reaches its maximum value within 0.4009 s. Furthermore, the peak time of the measured fault current is 0.4075 s and detection time is lower than this. Also, during the freewheel stage, when the capacitor delivers the discharge current, an extremely high magnitude of fault current can be ten times the nominal value and rises rapidly.

Based on the simulation results, this method prevents damaging vulnerable components such as IGBTs in the VSC and enables rapid PP fault detection.

2) *PG Faults Detection*: Figure 12 presents the fault currents as seen by relay R for different simulated PG faults at different locations and with different R_f . The PP fault occurs at $t_0 = 0.4$ s. The proposed method can detect faults with a very high resistance ($0-20 \Omega$). In case of DC lines, faults with R_f higher than 20Ω are not common and not very dangerous, so they can be detected by other, slower protection schemes. The fault at the battery line (location F4) with $R_f=20 \Omega$ is the most challenging in the considered DC radial microgrid and is detected in the 503rd window, as shown in Figure 13. Based on the simulations for lower fault resistances, PG faults are detected between 500th and 502nd window which confirms that the proposed method is fast and reliable.

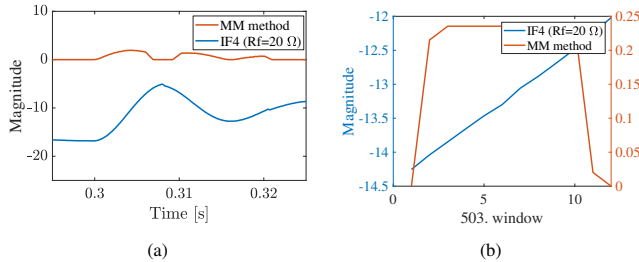


Figure 13: Results of the most sensitive case – PG fault simulation: (a) MM method applied to the fault occurred at F4 - battery line ($R_f=20 \Omega$), (b) time window for the fault detection

In case of a PG fault at 10% of the VSC line with fault

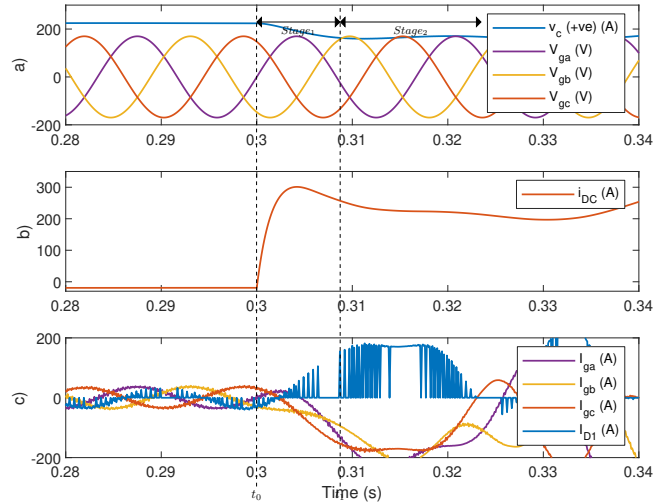


Figure 14: PG fault at the VSC line. a) DC link positive voltage $v_{c(+ve)}$ and three-phase grid-side voltages V_{ga} , V_{gb} , V_{gc} b) Current over the VSC line i_{DC} c) Diode current I_{D1} and three-phase grid-side currents I_{ga} , I_{gb} , I_{gc}

resistance 0.05Ω , the current of the VSC line experiences a transient of 320 A, as can be seen in Figure 14. The PG fault occurs at $t_0 = 0.3s$. $v_{c(+ve)}$ is the positive voltage of the DC-link capacitor, i_{DC} is the fault current equal to the sum of the current of the DC-link capacitor and the line current before the VSC DC-link capacitor. I_{D1} is the diode current of the VSC, while V_{ga} , V_{gb} and V_{gc} are three-phase grid voltages. Fault currents (IF1, IF2, IF3 and IF4) are measured at the relay point (R) on the VSC line.

3) *PP and PG Faults Contribution of the DC Source Elements*: Figure 15 shows fault contributions of the battery and the PV system ($I_{battery_out}$ and I_{PV_out}) and their currents in the input of the bidirectional converter and of the PV's boost converter ($I_{battery_in}$ and I_{PV_in}) for the system operating point used in the case study (insulation of PV power is 1000 Wp/m^2 , and power sharing to the main AC grid 8 kW). In the normal conditions, the I_{PV_out} is around 13 A, while the battery is discharges at around 12 A. In this case, the fault detection is sufficient, as shown in the above subsections IV-C1 and IV-C2. Battery has a lower contribution to the fault as compared to the PV source. Naturally, a battery with higher capacity would have higher fault contribution. Increase in the time constant of the fault current supplied from the PV and the battery is a result of an additional inductance of the distribution line. During the PG faults at the VSC line and the DC busbar, the currents of the battery and the PV system are also affected by this disturbance, although not significantly. Compared to the PP faults, oscillations in the PG fault currents are more obvious.

D. Simulation Results for Different Systems Operating Points

Fault contribution of the PV system will be further decreased at lower irradiation, adding another challenge in identifying the fault current contributed from such sources. We simulate these scenarios to determine the robustness of the proposed method for different operating points. The first scenario is simulated for a PG fault at location F2 (DC busbar) when the irradiation of the PV system is reduced to 250

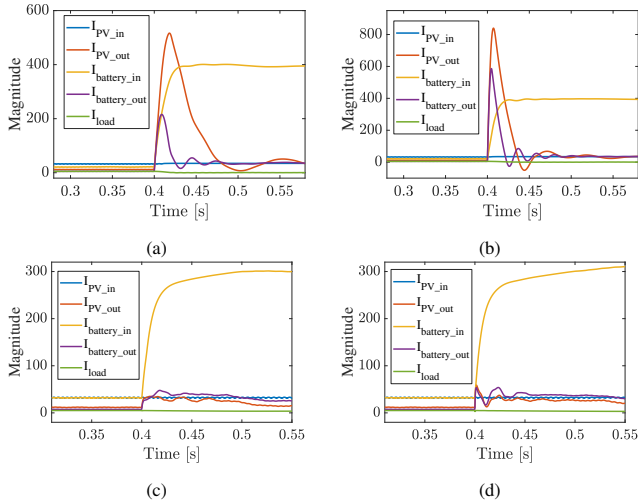


Figure 15: Results of the PP and PG fault simulations and contributions of the DC sources at the nominal operating point: (a) PP fault at the VSC line – F1 location, (b) PP fault at the DC busbar – F2 location, (c) PG fault at the VSC line – F1 location ($R_f = 2 \Omega$), (d) PG fault at the DC busbar – F2 location ($R_f = 2 \Omega$)

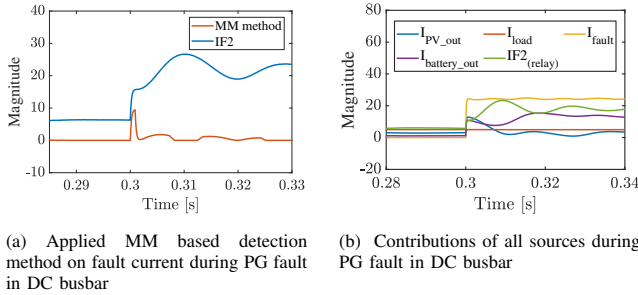


Figure 16: Simulation results for case 1 - fault is simulated in DC busbar, PV works on 25% of rated power and sharing power from the AC grid ($P_{ref}=3\text{kW}$)

Wp/m^2 , and the power is sent from the AC grid (Figure 16). The second scenario includes power sharing to the main AC grid (when there is a surplus of energy) including a change in the power reference shared between the DC microgrid and the AC grid, from 4.5 kW to 7.5 kW (Figure 17). Fault currents (IF2 and IF1_50%) are measured at relay point (R), which is located at the VSC line, and the proposed detection method will recognize these events as faults.

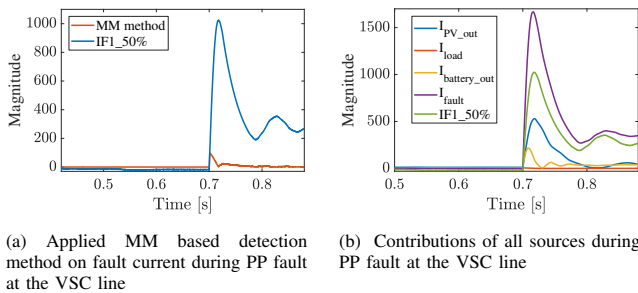


Figure 17: Simulation results for case 2 – the fault is simulated at 50% of the VSC line, sharing power to the AC grid ($P_{ref}=4.5\text{kW}$ and at the 0.52s $P_{ref}=7.5 \text{ kW}$)

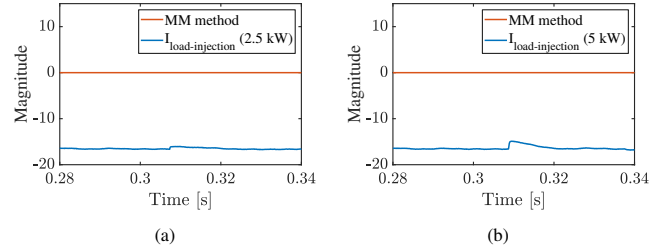


Figure 18: Simulation results for sudden load changes: (a) Injection of addition load (2.5 kW), (b) Injection of addition load (5 kW)

E. Simulation Results for Non-Fault Disturbance Events

We performed simulations for the most sensitive cases to show that the selected threshold is sufficient to distinguish faults from other disturbances. In Figure 18a the load of 2.5 kW is doubled (load is changed for 100%), and in Figure 18b the same load is tripled (load is changed for 200%). Fault currents ($I_{load-injection} (2.5 \text{ kW})$ and $I_{load-injection} (5 \text{ kW})$) measured at the relay point (R), located at the VSC line, will not recognize these events as faults. The slope of the current and the change in the current magnitude are much lower than in the case of the most critical HIF.

F. Computation Time

The MM-based algorithms are written and applied to the current signals in MATLAB. The algorithms of the denoising and detection methods are written in MATLAB R2021b and computed on the Intel Core i5 CPU with 4.0 GB of RAM. Since the speed of an algorithm depends on computer hardware and is not an intrinsic feature of the algorithm, the complexity should be quantified using the intrinsic time requirements. The MM operators have fast and straightforward calculations using only addition, subtraction, maximum and minimum operations without any multiplication and division during the signal processing, unlike FFT and WT. Since the algorithm uses simpler mathematical calculations than algorithms on digital protection relays for power systems, and the vendors declare speed of computation for their relays in ms, we decided to test the algorithm speed also in ms. The algorithm speed and memory usage were tested on the National Instruments RT controller with FPGA hardware. The algorithm speed was under 0.03 ms and memory usage was under 1 percent. This means that the algorithm can easily operate in real time (on this specific hardware) since the sampling frequency is 10 kHz. On top of this, MM uses a much smaller size of the sampling window (12 measured points, double-precision) in real-time signal processing, which is different from the integral transform-based algorithms that require longer windows which increase the computation burden. Also, there is no additional delay in operation because of the utilization of local measurements. As a result, the complexity of the calculation process is reduced and there is no need for dedicated hardware systems.

G. Guidelines for Experimental Setup

The paper does not present an experimental setup, however, we want to discuss challenges and directions regarding

the practical implementation that users may encounter when adapting this technique. The introduced protection algorithm is based on measurement from a single point. In this regard, the algorithm is resilient to communication delays and failures. However, for practical implementation the user can encounter problems regarding the response time of the transducer used for current measurements if the response time is slower than 1 ms. DC current can be measured by a current transducer such as Hall effect devices. The main prerequisite for practical application of the proposed protection algorithm is the use of a transducer for the current measurements with response time well below 1 ms.

V. CONCLUSION

The paper presented a fast fault detection method for radial DC microgrids. The method uses mathematical morphology denoising filters and local measurements. Since local measurements are used, it is resistant to communication delays and failures. The case study demonstrates that the proposed method distinguishes PP and PG short circuit faults from no-fault disturbance events, thus avoiding miss-operation of protection relays and satisfying the reliability. Numerous simulation studies have proved accuracy and effectiveness of the presented fault detection scheme. Finally, the proposed method is cost-effective since it does not require a dedicated specially-designed protection relay. In fact, any digital signal processing hardware with good speed and real-time operating system can be used. Compared with the traditional and frequency-based fault detection methods in DC microgrids, the proposed one is improved in view of relatively low sampling frequency, high fault resistance tolerance, and robustness against noise. In future studies, other aspects of fault management, such as fault location, identification and isolation will be investigated. Another line of research will be directed to other DC microgrid topology types, i.e. ring and mesh.

REFERENCES

- [1] J. Li, Y. Li, L. Xiong, K. Jia and G. Song, "DC Fault Analysis and Transient Average Current Based Fault Detection for Radial MTDC System," *IEEE Trans. Power Deliv.*, vol. 35, no. 3, pp. 1310-1320, June 2020.
- [2] S. Sarangi, B. K. Sabu, and P. K. Rout, "A comprehensive review of distribution generation integrated DC microgrid protection: issues, strategies, and future direction," *Int. J. Energy Res.*, vol. 45, no. 4, pp. 5006-5031, 2021.
- [3] A. Hooshya, R. Iravani, "Microgrid protection," *Proc. IEEE*, vol. 105, no. 7, pp. 1332-1353, 2017.
- [4] Z. Ali et al, "Fault Management in DC Microgrids: A Review of Challenges, Countermeasures, and Future Research Trends," *IEEE Access*, vol. 9, pp. 128032-128054, 2021.
- [5] R. Lazzari, and L. Piegari, "Design and implementation of LVDC hybrid circuit breaker," *IEEE Trans. Ind. Electron.*, vol. 34, no. 8, pp. 7369-7380, 2018.
- [6] S. Liu, P. Hu, D. Jiang, Y. Liang, and J. Zhuang, "A fast LVDC vacuum hybrid circuit breaker: Dielectric recovery and design consideration," *IET Gener. Transm. Distrib.*, vol. 15, no. 21, pp. 3058-3065, 2021.
- [7] J. Mohammadi, F. B. Ajaei, and G. Stevens, "Grounding the DC microgrid," *IEEE Trans. Ind. Appl.*, vol. 55, no. 5, pp. 4490-4499, 2019.
- [8] E. W. Nahas, H. A. Abd el Ghany, D.-E. A. Mansour, and M. Eissa, "Extensive analysis of fault response and extracting fault features for DC microgrids," *Alex. Eng. J.*, vol. 60, no. 2, pp. 2405-2420, 2021.
- [9] D. Salomonsson, L. Soder, and A. Sannino, "Protection of Low-Voltage DC Microgrids," *IEEE Trans. Power Deliv.*, vol. 24, no. 3, pp. 1045-1053, 2009.
- [10] J. Škare and M. Mesić, "Protection devices and selectivity in DC power distribution sub-systems," *J. Energy: Energija*, vol. 58, no. 1, pp. 76-97, 2009.
- [11] N. Bayati, H. R. Baghaee, M. Savaghebi, A. Hajizadeh, M. Soltani, and Z. Lin, "EMD/HT-based local fault detection in DC microgrid clusters," *IET Smart Grid*, vol. 5, no. 3, pp. 177-188, 2022.
- [12] S. Dhar, R. K. Patnaik, and P. K. Dash, "Fault Detection and Location of Photovoltaic Based DC Microgrid Using Differential Protection Strategy," *IEEE Trans. Smart Grid*, vol. 9, no. 5, pp. 4303-4312, 2018.
- [13] J.-D. Park and J. Candelaria, "Fault Detection and Isolation in Low-Voltage DC-Bus Microgrid System," *IEEE Trans. Power Deliv.*, vol. 28, no. 2, pp. 779-787, 2013.
- [14] W. Javed and D. Chen, "Low voltage DC microgrid protection system-A review," in *53rd International Universities Power Engineering Conference (UPEC)*, Glasgow, UK, September 4-7, 2018.
- [15] V. A. Lacerda, R. M. Monaro, D. Campos-Gaona, D. V. Coury, and O. Anaya-Lara, "Distance protection algorithm for multiterminal HVDC systems using the Hilbert-Huang transform," *IET Gener. Transm. Distrib.*, vol. 14, no. 15, pp. 3022-3032, 2020.
- [16] I. Grcić, H. Pandžić, and D. Novosel, "Fault Detection in DC Microgrids Using Short-Time Fourier Transform," *Energies*, vol. 14, no. 2, p. 277, 2021.
- [17] E. M. Amiri and B. Vahidi, "Integrated protection scheme for both operation modes of microgrid using S-Transform," *Int. J. Electr. Power Energy Syst.*, vol. 121, p. 106051, 2020.
- [18] S. Som and S. R. Samantaray, "Wavelet based fast fault detection in LVDC micro-grid," in *7th International Conference on Power Systems (ICPS)*, Pune, India, December 21-23, 2017.
- [19] H.-C. Seo, "Development of New Protection Scheme in DC Microgrid Using Wavelet Transform," *Energies*, vol. 15, no. 1, p. 283, 2022.
- [20] W. C. Shen, Y. H. Chen and A. Y. A. Wu, "Low-complexity sinusoidal-assisted EMD (SAEMD) algorithms for solving mode-mixing problems in HHT," *Digit. Signal Process.*, vol. 24, pp. 170-186, 2014.
- [21] N. K. Sharma, R. Pattanayak, S. R. Samantaray, and C. N. Bhende, "A Fast Fault Detection Scheme for Low Voltage DC Microgrid," in *21st National Power Systems Conference (NPSC)*, Gandhinagar, India, December 17-19, 2020.
- [22] T. Liu, Z. Luo, J. Huang, and S. Yan, "A comparative study of four kinds of adaptive decomposition algorithms and their applications," *Sensors*, vol. 18, no. 7, p. 2120, 2018.
- [23] M. Mishra, R. R. Panigrahi, and P. K. Rout, "A combined mathematical morphology and extreme learning machine techniques based approach to micro-grid protection," *Ain Shams Eng. J.*, vol. 10, no. 2, pp. 307-318, 2019.
- [24] R. Godse and S. Bhat, "Mathematical morphology-based feature-extraction technique for detection and classification of faults on power transmission line," *IEEE Access*, vol. 8, pp. 38459-38471, 2020.
- [25] T. Gush, S. B. A. Bukhari, R. Haider, S. Admasie, Y.-S. Oh, G.-J. Cho, and C.-H. Kim, "Fault detection and location in a microgrid using mathematical morphology and recursive least square methods," *Int. J. Electr. Power Energy Syst.*, vol. 102, pp. 324-331, 2018.
- [26] M. Ashouri, F. Faria da Silva, and C. Leth Bak, "Analysis and validation of mathematical morphology filters for single-ended fault localization in VSC-HVDC links," *Electr. Eng.*, vol. 103, no. 3, pp. 1583-1596, 2021.
- [27] V. Raghpoor, M. Mehrabi-Kooshki, and R. Razzaghi, "A novel non-unit protection scheme for HVDC transmission lines based on multi-resolution morphology gradient," *IET Gener. Transm. Distrib.*, vol. 15, no. 5, pp. 894-911, 2020.
- [28] M. A. Farhan and K. S. Swarup, "Mathematical morphology-based islanding detection for distributed generation," *IET Gener. Transm. Distrib.*, vol. 10, no. 2, pp. 518-525, 2016.
- [29] F. Ghalavand, B. A. M. Alizade, H. Gaber, and H. Karimipour, "Microgrid islanding detection based on mathematical morphology," *Energies*, vol. 11, no. 10, p. 2696, 2018.
- [30] K. Sekar and N. K. Mohanty, "Data mining-based high impedance fault detection using mathematical morphology," *Comput. Electr. Eng.*, vol. 69, no. 10, pp. 129-141, 2018.
- [31] A. Khan, B.-h. Wang, I. Tariq and S. R. Abbas "A Comparative Study of Morphological Gradient and Its Improved Form for CT Saturation Detection," in *2nd International Conference on Wireless Communication and Network Engineering (WCNE 2017)*, Xiamen, China, December 24-25, 2017.
- [32] I. D. Saputra, "Detection of Power Disturbances for Power Quality Monitoring Using Mathematical Morphology," PhD Dissertation, University of Liverpool, England, 2017.

- [33] Y. M. Yeap, N. Geddada, K. Satpathi, and A. Ukil, "Time- and Frequency-Domain Fault Detection in a VSC-Interfaced Experimental DC Test System," *IEEE Trans. Industr. Inform.*, vol. 14, no. 10, pp. 4353-4364, 2018.
- [34] H. M. Maruf, F. Kamal, and B. H. Chowdhury, "Mathematical morphological filter based protection scheme for DC ring microgrid system," in *Proc. of North American Power Symposium (NAPS)*, Fargo, ND, USA, September 9-11, 2018.
- [35] Y.-S. Oh, J. Han, G.-H. Gwon, D.-U. Kim, C.-H. Noh, C.-H. Kim, T. Funabashi, and T. Senjyu, "Detection of high-impedance fault in low-voltage DC distribution system via mathematical morphology," *J. Int. Counc. Electr. Eng.*, vol. 6, no. 1, pp. 194-201, 2016.
- [36] N. Bayati, A. Hajizadeh, and M. Soltani, "Protection in DC microgrids: a comparative review," *IET Smart Grid*, vol. 1, no. 3, pp. 66-75, 2018.
- [37] S. Beheshtaein, R. M. Cuzner, M. Forouzes, M. Savaghebi, and J. M. Guerrero "DC microgrid protection: A comprehensive review," *IEEE Trans. Emerg. Sel. Topics Power Electron.*, early access.
- [38] K. A. Saleh, A. Hooshyar and E. F. El-Saadany, "Ultra-High-Speed Traveling-Wave-Based Protection Scheme for Medium-Voltage DC Microgrids," in *IEEE Trans. Smart Grid*, vol. 10, no. 2, pp. 1440-1451, March 2019.
- [39] N. Bayati, H. R. Baghaee, A. Hajizadeh, M. Soltani, and Z. Lin, "Mathematical morphology-based local fault detection in DC Microgrid clusters," *Electr. Power Syst. Res.*, vol. 192, p. 106981, 2021.
- [40] J. Yang, J. E. Fletcher, and J. O'Reilly, "Short-circuit and ground fault analyses and location in VSC-based DC network cables," *IEEE Trans. Ind. Electron.*, vol. 59, no. 10, pp. 3827-3837, 2011.
- [41] S.D. Fletcher, P.J. Norman, S.J. Galloway, P. Crolla, G.M. Burt, "Optimizing the roles of unit and non-unit protection methods within DC microgrids," *IEEE Trans. Smart Grid*, vol. 3, no.4, pp. 2079-2087, 2012.
- [42] Y.-S. Oh, C.-H. Kim, G.-H. Gwon, C.-H. Noh, S. B. A. Bukhari, R. Haider, and T. Gush, "Fault detection scheme based on mathematical morphology in last mile radial low voltage DC distribution networks," *Int. J. Electr. Power Energy Syst.*, vol. 106, pp. 520-527, 2019.
- [43] S. Gautam and S. M. Brahma, "Guidelines for selection of an optimal structuring element for mathematical morphology based tools to detect power system disturbances," in *Proc. of IEEE Power and Energy Society General Meeting*, San Diego, CA, USA, July 22-26, 2012.
- [44] Q.-H. Wu, Z. Lu, and T. Ji, "Protective relaying of power systems using mathematical morphology," *Springer Science & Business Media*, 2009.
- [45] J. Yu , T. Hu, H. Liu, "A new morphological filter for fault feature extraction of vibration signals," *IEEE Access*, vol. 7, pp.3743-3753, 2019.
- [46] K. Saleh, "Protection of multi-terminal remote DC microgrids with overhead lines against temporary and permanent faults," *IET Generation, Transmission & Distribution*, vol. 14, no. 15, pp. 2879-2889, 2020.
- [47] Low Voltage Directive (LVD), ec.europa.eu/growth/sectors/electrical-and-electronic-engineering-industries-eei/low-voltage-directive-lvd_en, 05 04 2022.
- [48] J. Rocabert, A. Luna, F. Blaabjerg, and P. Rodriguez, "Control of power converters in AC microgrids," *IEEE Trans. Power Electron.*, vol. 27, no. 11, pp. 4734-4749, 2012.
- [49] T. Dragičević, X. Lu, J. C. Vasquez, and J. M. Guerrero, "DC microgrids—Part II: A review of power architectures, applications, and standardization issues," *IEEE Trans. Power Electron.*, vol. 31, no. 5, pp. 3528-3549, 2015.
- [50] B. Perea-Mena, J. A. Valencia-Velasquez, J. M. López-Lezama, J. B. Cano-Quintero, and N. Muñoz-Galean, "Circuit Breakers in Low-and Medium-Voltage DC Microgrids for Protection against Short-Circuit Electrical Faults: Evolution and Future Challenges," *Appl. Sci.*, vol. 12, no. 1, pp. 3528-3549, 2021.